Engineering the Hybrid Interfaces in Ladder-Like Polysilsesquioxane/Al_2O_3 Nanocomposites for Enhancing Thermal Conductivity

Chiara Romeo[a,], Emanuela Callone[a,b], Riccardo Ceccato[a], Francesco Parrino[a], Giulia Fredi[a], Alessandra Vitale[c,d], Ignazio Roppolo[c], Roberta Bongiovanni[c,d], Massimiliano D'Arienzo[e], Sandra Dirè[a,b,*]*

[a] Department of Industrial Engineering, University of Trento, via Sommarive 9, 38123 Trento, Italy

[b] "Klaus Müller" Magnetic Resonance Lab., Department of Industrial Engineering, University of Trento, Via Sommarive 9, 38123 Trento, Italy

[c] Department of Applied Science and Technology, Politecnico di Torino, Corso Duca degli Abruzzi 24, 10129 Torino, Italy

[d] INSTM UdR Politecnico di Torino, Via G. Giusti 9, 50121 Firenze, Italy

[e] Department of Materials Science, University of Milano - Bicocca, Via R. Cozzi 55, 20125 Milano, Italy

* Corresponding authors: C. Romeo, chiara.romeo@unitn.it, S. Dirè, sandra.dire@unitn.it

Abstract

The potential of ladder-like polysilsesquioxanes (LPSQs) combined with thermally conductive fillers for developing nanocomposites (NCs) with enhanced thermal conductivity (TC) has recently gained interest. While early studies emphasize the importance of controlling ladder–filler interactions, the role of the hybrid interface on interfacial thermal resistance and TC remains underexplored. To address this gap, novel photocurable NCs were developed by incorporating Al_2O_3 nanoparticles (NPs) functionalized with methacrylate (MA) or amino (AA) groups into LPSQs bearing methacrylate and phenyl side chains. Characterizations revealed that methacrylate conversion and crosslinking significantly affect TC. Furthermore, the nature of covalent and non-covalent interactions at the ladder-filler interface influences both LPSQs structural organization and NCs thermal behavior. Among unfilled matrices, methacrylate-rich polysilsesquioxane (LPMASQ) displays the highest TC due to effective crosslinking. MAPSQ(46), with a 40/60 methacrylate-to-phenyl ratio, shows slightly lower TC, where reduced polymerization was offset by π–π stacking that promotes heat transfer. The introduction of MA NPs improves TC in all systems, particularly in LPMASQ, where copolymerization with the matrix reduces interfacial thermal resistance. Conversely, AA NPs, with lower dispersibility and weaker interactions, affect chain organization in LPMASQ, introducing phonon scattering and lowering TC. However, in mixed LPSQs like MAPSQ(64), with a 60/40 methacrylate-to-phenyl ratio, amino groups enhance thermal diffusivity, suggesting that weak interactions can be beneficial in matrices with limited polymerization. These results underscore the critical role of tuning both LPSQs side chain composition and NPs surface functionalization to balance interfacial interactions and maximize thermal performance in polymer NCs for advanced thermal management applications.

Keywords: thermal conductivity; ladder-like polysilsesquioxanes; polymer nanocomposites; weak interactions; crosslinking; hybrid interface; nanoparticles functionalization.

1. Introduction

As electronic components become smaller and more power-dense, the demand for materials with efficient heat dissipation capabilities has significantly increased. Efficient thermal management in electronic devices requires precise control over several material properties, such as thermal conductivity (TC), thermal and mechanical stability, electrical insulation, and flexibility.

In polymers, heat transfer primarily occurs via phonon transport, where molecular vibrations propagate energy [1]. The TC of polymers is strongly influenced by the chain structure, with rigid chains, double bonds, or aromatic rings typically enhancing the TC due to stronger inter-chain interactions [2]. As crystallinity increases the structural order, semi-crystalline polymers typically exhibit higher TC, whereas amorphous polymers, with random chain conformations, experience greater phonon scattering and lower TC. Crosslinking also improves TC by creating stable, covalently bonded networks that restrict chain mobility, promoting heat transfer, as observed in thermosetting polymers such as epoxy resins [3, 4]. Weak interactions, such as hydrogen bonds, π-π stacking, and van der Waals forces also affect TC. For instance, hydrogen bonding in polyamide-based composites enhances phonon transfer, thereby increasing TC [5], while weak Van der Waals forces can hinder phonon mobility [6, 7]. On the other hand, π-π interactions can facilitate the formation of thermally conductive networks that improve heat dissipation, as reported for composite materials containing graphene as the filler [8].

The incorporation of ceramic fillers is a widely employed strategy to enhance the TC of polymers [6]. However, the filler-matrix interface plays a critical role in determining the TC of the composite, as poor interfaces cause thermal resistance and phonon scattering [9]. Functionalizing nanoparticles to introduce filler-matrix interactions can improve the filler dispersion and reduce the interfacial thermal resistance, leading to enhanced TC [8, 10]. Optimizing such interactions is a key strategy for developing advanced polymer-based thermal management materials (TMMs); however, their effectiveness strongly depends on the polymer-filler combination and the material morphology, thus requiring further research to quantify their impact across different systems.

Ladder polysilsesquioxanes (LPSQs) are a class of hybrid organic-inorganic polymers characterized by a double-stranded ladder structure, synthesized through hydrolysis–condensation reactions of trifunctional silane monomers. Their backbone consists of silicon (Si) and oxygen (O) atoms, having the chemical formula $[RSiO_{1.5}]_n$, with organic R groups attached to the silicon atoms [11, 12]. Unlike random [13] or cage-like polysilsesquioxanes [14], the linear structure of LPSQs imparts unique properties, including high thermal stability, mechanical strength, resistance to environmental degradation, excellent dielectric properties, and the ability to form stable and uniform films [15, 16, 17]. These characteristics make LPSQs suitable for a wide range of applications, including advanced coatings [18], energy devices[19], and electronics [20, 21]. In a previous study by some of the authors, the positive influence of the addition of LPSQs on the mechanical, thermal, and dielectric properties of polymer composites was explored [20]. However, their potential as TMMs has only recently attracted attention [15]. Due to their low thermal expansion coefficients, moderate TC, and excellent dimensional stability, LPSQs offer promising solutions for dissipating heat and mitigating stress, thereby boosting devices' durability and performance. In this framework, our group has recently proposed the use of photocurable ladder

polymethacrylate silsesquioxanes (LPMASQ) in combination with alumina nanoparticles (Al_2O_3 NPs) to develop flexible nanocomposites with remarkable TC [22, 23]. These studies examined how polymer chain configuration, crosslinking degree, and nanoparticle surface functionalization affect the TC of LPMASQ–Al_2O_3 nanocomposites. These preliminary results highlighted the potential of LPSQs in developing thermally conductive polymers suitable for heat dissipation and pointed out that the fabrication of advanced TMMs can result from the modulation of ladder-filler interactions. Therefore, the modification of organic end groups in LPSQs in combination with tailored filler functionalization appears to be a promising approach for the optimization of the thermal management performance.

In the present research we developed photocurable nanocomposites (NCs), comprised of LPSQs-based polymeric matrices embedded with functionalized Al_2O_3 NPs. The primary objective was to correlate the TC of the NCs with the interface properties, by studying the effect of the polymer-filler interactions on the phonon transmission. To this aim, LPSQs bearing only methacrylate groups or both methacrylate and phenyl groups in different ratios were prepared. The methacrylate groups in LPSQs provide reactive sites for covalent crosslinking, thereby enhancing mechanical strength, chemical resistance, UV-curing capabilities, adhesion, and scratch resistance [24–27]. On the other hand, the aromatic nature of phenyl groups is supposed to increase the rigidity of the polymer backbone, and promote weak π-π interactions [28–31]. Photocrosslinked LPSQs were thoroughly characterized by means of Fourier transform infrared spectroscopy (FTIR), solid-state nuclear magnetic resonance (SS-NMR), X-ray diffraction (XRD), and real-time photorheology experiments. Likewise, Al_2O_3 NPs were functionalized with both methacryloxypropyl trimethoxysilane (MPTMS) and aminopropyl trimethoxysilane (APTMS) to study the effect of surface groups that establish different interactions with LPSQs. In particular, NPs functionalized

with methacrylate groups can develop covalent interactions improving phonon transfer from the ceramic NPs to the matrix, while amino-functionalized NPs can interact with methacrylate and phenyl side chains of LPSQs through various weak interactions, such as H-bonding and van der Waals forces. NCs were prepared by adding variable amounts of functionalized Al_2O_3 NPs to the LPSQs matrices; they were cured through photopolymerization, and characterized by FTIR, SS-NMR, XRD, scanning electron microscopy (SEM), thermogravimetric analysis (TGA), and photorheology experiments. The thermal diffusivity values were obtained using Laser Flash Analysis (LFA), and the TC values were subsequently calculated by measuring the corresponding density and specific heat capacity values. The changes in TC were correlated with the interfacial interactions developed by the functional groups in LPSQs and NPs surface, which in turn affected both crosslinking and structural properties of the NCs.

2. Materials and Methods

2.1 Materials

Gamma alumina nanoparticles (99.5%, NanoArcTM, AL-0405, average particles diameter 48 nm, specific surface area SSA 34 $m^2 \cdot g^{-1}$) were obtained from Alfa Aesar (Haverhill, MA, USA). 3-Methacryloxypropyl trimethoxysilane (98%, MPTMS) was obtained from ABCR GmbH (Karlsruhe, Germany). Phenyl trimethoxysilane (98%, PTMS) and aminopropyl trimethoxysilane (99%, APTMS) were obtained from Sigma Aldrich (St. Louis, MO, USA). Ethanol absolute anhydrous (EtOH ≥ 99.9%) was purchased from Carlo Erba reagents (Milan, Italy). Toluene (99.8%), tetrahydrofuran (99.9%, THF), potassium carbonate (K_2CO_3 ≥ 99.0%), and 1-hydroxycyclohexyl phenyl ketone (99%, Irgacure 184, I-184) were purchased from Sigma-Aldrich (St. Louis, MO, USA).

2.2 Sample Preparation

2.2.1. Synthesis of LPSQs. The ladder-like polysilsesquioxanes were prepared from trialkoxysilanes by the sol–gel process [20, 25, 28]. Poly(propylmethacrylate)silsesquioxanes (LPMASQ) were prepared using MPTMS; poly(propylmethacrylate-phenyl) silsesquioxanes MAPSQ(64), and MAPSQ(46) were obtained from mixtures of MPTMS and PTMS, in a molar ratio of 6:4 and 4:6, respectively. Briefly, for the preparation of LPMASQ, 0.08 mol of MPTMS were added dropwise in a mixture of H_2O (4.8 ml) and THF (9.1 ml) in the presence of 0.04 g of K_2CO_3 as catalyst, under nitrogen flow. The viscous solution was stirred vigorously at room temperature for 240 hours under N_2 atmosphere, avoiding exposure to light. The solvent was then evaporated at 30 °C under mild vacuum conditions, yielding a transparent, glue-like product. MAPSQ(64) and MAPSQ(46) were prepared following the same procedure, but reducing the reaction time to 96 hours and using a mixture of MPTMS and PTMS: 0.048 mol and 0.032 mol for MAPSQ(64), and vice versa for MAPSQ(46), respectively. The final products were then kept in a desiccator in N_2 atmosphere in the dark. A schematic representation of the synthetic procedure is detailed in Supporting information, Scheme S1.

2.2.2. Synthesis of functionalized alumina NPs. MPTMS-capped Al_2O_3 nanoparticles, labelled as MA, and APTMS-capped Al_2O_3 nanoparticles, labelled as AA, were synthesized according to our previous report [23]. In detail, 2 g of gamma nano-Al_2O_3 were dispersed in 50 mL of toluene by sonication for 15 min and then put under reflux conditions. MPTMS (830 μL), or APTMS (608 μL), were added dropwise, and the suspensions were vigorously stirred and kept under reflux at 120 °C for 24 h (Scheme S2, Supporting information). The functionalized nanoparticles were collected by centrifugation at 4500 rpm for 15 min, washed twice with toluene and once with ethanol, and finally dried in a vacuum oven at 80 °C overnight.

2.2.3. Preparation of LPSQs/Al_2O_3 nanocomposites. Nanocomposites made of different LPSQs (Section 2.2.1) and variable amounts of MA and AA nanoparticles were prepared by solvent casting and photocuring, as reported in our previous work [23]. Table 1 reports the prepared nanocomposites alongside their corresponding alumina weight fractions (Al_2O_3 wt.%, with respect to the matrix) and volume fractions (Al_2O_3 vol%) for all samples. Herein is briefly reported the procedure for LPMASQ nanocomposites filled with MA particles; the same procedure was applied for all other composites, varying the type of matrix and particles. LPMASQ (1 g) was dissolved at room temperature in 1 mL of THF. Variable amounts of MA (i.e. 20, 40, 80, and 120 wt.% with respect to the matrix) were suspended by sonication (15 min) in 2 mL of THF and then added, under vigorous stirring, into the matrix solution. Finally, 50 mg of I-184 photoinitiator (5 wt.% with respect to LPMASQ) were dissolved in THF (0.5 mL) and then added to the sample solutions. The mixtures were stirred in the dark for 30 min and then poured into polypropylene Petri dishes. The solvent was evaporated in an oven at 30 °C under a mild vacuum for 2 h, avoiding exposure to light. LPMASQ-based dried samples, namely the pure matrix and the composites, were photocrosslinked into a cooled isolated chamber using a mercury vapor lamp (HBO 50 W/AC 39 V, OSRAM, specimen–lamp distance 13 cm, curing time 15 min, lamp intensity 3 $mW \cdot cm^{-2}$), under N_2 flow to avoid oxygen inhibition at the surface. Samples were maintained at about 6°C during UV-induced crosslinking, an optimized condition that ensured complete polymerization while preventing thermal damage and surface stickiness. The specimens were irradiated for 10 min on the upper side and then for 5 min on the lower side to improve the homogeneity of the photocrosslinking reaction. The obtained films (approximately 300 μm thick) were stored in a desiccator, in the dark, and under a N_2 atmosphere. Selected samples were prepared in triplicate and characterized by the techniques reported in the following section. The described procedure is

schematized in Supporting information, Scheme S3. Figure S1 shows two images of representative cured samples.

LPMASQ-based NCs were labelled as XMA_L and XAA_L, where L is the matrix and X is the weight fraction of MA or AA particles (i.e., from 20 to 120 wt.%) added with respect to the matrix; likewise, MAPSQ(64)-based NCs were labelled as XMA_M(64) and XAA_M(64), and MAPSQ(46)-based NCs were labelled as XMA_M(46) and XAA_M(46).

Table 1. Labelling and composition of the prepared nanocomposites.

NCs Class	Matrix type	NPs type	Sample ID	Al_2O_3 wt.%	Al_2O_3 vol%
MA_L	LPMASQ	MA	20MA_L	20	8.0
			40MA_L	40	15.2
			80MA_L	80	27.5
			120MA_L	120	35.5
AA_L	LPMASQ	AA	20AA_L	20	7.5
			40AA_L	40	14.2
			80AA_L	80	24.6
			120AA_L	120	33.0
MA_M(64)	MAPSQ(64)	MA	20MA_M(64)	20	8.7
			40MA_M(64)	40	16.1
			80MA_M(64)	80	28.0
			120MA_M(64)	120	38.1
AA_M(64)	MAPSQ(64)	AA	20AA_M(64)	20	7.8
			40AA_M(64)	40	14.3
			80AA_M(64)	80	25.4
			120AA_M(64)	120	32.8
MA_M(46)	MAPSQ(46)	MA	80MA_M(46)	80	28.0
AA_M(46)	MAPSQ(46)	AA	80AA_M(46)	80	24.3

2.3 Characterization Techniques

Real-time Fourier Transform Infrared (rt-FTIR) spectroscopy was used to analyze the photopolymerization kinetics of both the pristine matrices and the nanocomposites. The measurements were conducted using a Thermo Fisher Scientific Nicolet™ iS50 spectrometer in transmission mode, covering the spectral range of 2700–650 cm^{-1}. Thin films of approximately 10 μm thickness were prepared by spreading the sample solutions onto silicon wafers with a wire wound applicator. A high-pressure mercury xenon lamp (LIGHTNINGCURE™ Spotlight source LC8, Hamamatsu) equipped with an optical fiber was positioned 7 cm above the samples to provide irradiation at an intensity of 7 $mW \cdot cm^{-2}$, as measured by a UV Power Puck® II radiometer (EIT® Instrument Markets). FTIR spectra were continuously recorded at a rate of 40 spectra per minute throughout the 360 s irradiation period, switching on the UV lamp after 60 s from the beginning of the rt-FTIR measurements. This exposure time differed from that used for the preparation of the nanocomposite films (Section 2.2.3) as a consequence of variations in film thickness and lamp intensity. To prevent oxygen inhibition at the surface, a 50 μm polyethylene film was placed over the samples. Three independent measurements were performed for each sample, and the results were averaged to determine the final conversion values over time, with an average standard deviation of 4%. The double bond conversion of the methacrylate group was calculated using equation 1:

$$Double\ bond\ conversion\ (\%) = (1 - A_t/A_0) \cdot 100 \qquad (1)$$

where A_t is the area of the peak of the methacrylate C=C double bonds at 1637 cm^{-1} at time t of irradiation and A_0 is the area of the same peak before irradiation. The areas of such peaks were normalized to the area of the methacrylate carbonyl stretching vibration at 1716 cm^{-1}, used as an

internal reference. The photopolymerization rate was derived from the first derivative of the curve of double bond conversion vs. time.

Real-time photorheology experiments were conducted using an Anton PAAR Modular Compact Rheometer (Physica MCR 302, Graz, Austria) in a parallel-plate configuration (25 mm diameter) with borosilicate bottom glass. The gap between the plates was set to 300 μm, and all tests were conducted under isothermal conditions at 25 °C. The viscoelastic properties of the photocurable formulations were monitored under a constant oscillation frequency (10 Hz) and strain amplitude (1%) within the linear viscoelastic region (LVR), as determined from preliminary amplitude sweep tests. A UV-light source (Hamamatsu LC8 lamp, 10 $mW \cdot cm^{-2}$) positioned beneath the bottom plate was used to initiate the photopolymerization reaction (specimen-lamp distance of 7 cm). UV exposure started 30 s after the start of the experiment to allow system stabilization. The evolution of the storage (G') and loss (G") moduli during irradiation provided insights into the crosslinking kinetics. All measurements were conducted in triplicate, and the results were averaged to ensure reproducibility. The UV lamp was switched off once the G' curve reached a plateau, resulting in a total measuring time of 4 min. This exposure time differed from that used for the preparation of the nanocomposite films (section 2.2.3) due to variations in the curing conditions.

FTIR analyses of the nanoparticles and photocrosslinked samples were performed using a Nicolet Avatar 330 spectrometer (Thermo Fisher Scientific, Waltham, MA, USA). Bare and functionalized alumina nanoparticles were analyzed in transmittance mode on KBr pellets in the 4000–400 cm^{-1} wavenumber range (64 scans, resolution 4 cm^{-1}). Photocrosslinked matrices and nanocomposites were characterized through attenuated total reflectance (ATR) FTIR spectroscopy. ATR spectra were acquired with a ZnSe crystal in the 4000–650 cm^{-1} wavenumber range (128 scans, resolution 4 cm^{-1}).

SS-NMR analyses were carried out on MA and AA particles, photocrosslinked matrices and nanocomposites using a Bruker 400WB spectrometer (^{1}H frequency 400.13 MHz). Samples were packed in 4 mm zirconia rotors and spun at 8 kHz under airflow. Si units are assigned according to the standard NMR nomenclature: T^n denotes a $SiCO_3$ unit, where n represents the number of bridging oxygens. Adamantane and Q_8M_8 served as external secondary references. The NMR experiments were conducted using both single-pulse and cross-polarization (CP) sequences under the following acquisition parameters: (i) ^{13}C NMR: 100.48 MHz, contact time 2 ms, decoupling length 5.9 μs, recycle delay 5 s, 2000 scans; (ii) ^{29}Si NMR: 79.48 MHz, contact time 5 ms, decoupling length 6.3 μs, recycle delay 10 s, 2000 scans. Single pulse sequence: π/4 pulse 3.9μs, recycle delay 300 s, 1000 scans.

XRD patterns were collected on crosslinked matrices and NCs with a Rigaku D/III max diffractometer (Rigaku Holdings Corporation, Tokyo, Japan), using Cu Kα1 radiation (λ = 1.54056 Å) and a curved graphite monochromator in the diffracted beam, in the 2θ range of 3°–40°, with a sampling interval of 0.05°, and a counting time of 4 s. Self-standing films were fixed directly to the Al holder with scotch tape. The profile fitting analysis of XRD patterns was performed using Jade8 software (Materials Data Inc., MDI, Livermore, CA, USA).

TGA analyses of functionalized alumina nanoparticles were performed using a Q5000 TA Instruments thermogravimetric analyzer from 30 °C to 850 °C at a heating rate of 10 °C/min under N_2 flow (10.0 mL/min). The thermal behavior of photocrosslinked matrices and nanocomposites was investigated through thermogravimetric experiments performed from 30 °C to 900 °C with a heating rate of 10 °C/min under air flow (15 mL/min), using a Mettler Toledo (Columbus, OH, USA) TG50.

Cross-sectional micrographs of the photocrosslinked nanocomposites were recorded with a Carl Zeiss (Oberkochen, Germany) Gemini Supra 40 field emission SEM, operating at 7.50 keV and using secondary electrons as the main source. The composite films were dipped in liquid N_2 prior to fracturing. A thin layer of metallic coating (Pt/Pd = 80/20) was sputtered onto the samples before SEM analysis.

Samples density (ρ) was evaluated at 25 °C using a Micromeritics (Norcross, GA, USA) Multivolume Helium Pycnometer AccuPyc 1330. Reported values represent the mean of three independent measurements, with a standard deviation not exceeding ±0.02 $g \cdot cm^{-3}$. The density value of bare Al_2O_3 powders was 3.08 ± 0.14 $g \cdot cm^{-3}$.

The specific heat capacities (c_P) of the alumina NPs and crosslinked matrices were evaluated at 25 °C using a Mettler Toledo (Columbus, OH, USA) 30 DSC, according to the ASTM E1269 standard. The samples were weighed and hermetically sealed in aluminum crucibles prior to analysis. Differential scanning calorimetry measurements were performed under a nitrogen flow of 50 mL/min, using a heating rate of 10 °C/min within a temperature range from −10 °C to 40 °C. Each c_P value corresponds to the average of three independent tests, with a maximum standard deviation of ±0.02 $J \cdot g^{-1} \cdot K^{-1}$. The c_P experimental values of the bare, AA, and MA particles were 0.78, 0.75, and 0.90 $J \cdot g^{-1} \cdot K^{-1}$, respectively. The measured specific heat values for the pristine matrices and NPs were subsequently used to estimate the specific heat of the nanocomposites through the rule of mixtures, as described in our previous work [22].

The thermal diffusivity (α) of the nanoparticles, photocrosslinked matrices, and nanocomposites was measured at 25 °C using a Netzsch (Selb, Germany) LFA 467 HyperFlash Light Flash Analyzer in an inert N_2 atmosphere. Solid films of crosslinked matrices and NCs (diameter 12.5 mm, thickness ~300 μm) were tested employing a laser voltage of 250 V and a pulse width of

30 µs, with five repeated measurements per specimen. To assess the diffusivity of the bare and functionalized Al_2O_3 nanopowders, a three-layer configuration was used: the powders were pressed between aluminum discs and clamped using a torque of 15 cN·m. These tests used a 600 µs pulse width and five pulses per sample. The Proteus® software (NETZSCH, version 8.0.3) was used for data analysis, implementing the three-layer method with a linear baseline and numerical pulse correction. The reported α values are the averages of three replicates with a maximum standard deviation of ±0.001 $mm^2 \cdot s^{-1}$.

The thermal conductivity (k) of the photocrosslinked matrices and composites was calculated using equation 2:

$$k = \rho \cdot c_P \cdot \alpha \qquad (2)$$

using experimentally derived values of density (ρ, $g \cdot cm^{-3}$), specific heat capacity (c_P, $J \cdot g^{-1} \cdot K^{-1}$), and thermal diffusivity (α, $mm^2 \cdot s^{-1}$). The uncertainty of k was calculated according to the Kline–McClintock model, with a standard deviation of ±0.001 $W \cdot m^{-1} \cdot K^{-1}$.

3. Results and Discussion

3.1 Structural characterization of LPSQs matrices with different organic pendant groups

Ladder-based NCs were prepared through solvent casting followed by UV-curing using three different matrices: LPMASQ with 100% of methacrylate groups as organic pendants, MAPSQ(64), which contains 60% of methacrylate groups and 40% of phenyl groups, and MAPSQ(46), with 40% of methacrylate groups and 60% of phenyl groups. They were synthesized via sol-gel chemistry according to an established protocol [22, 23]. Undamaged and slightly translucent discs were obtained for all ladder matrices (Figure S1a).

The structural characterization of the photocured ladders was performed by ATR-FTIR and SS-NMR spectroscopy. The ladder-like structure of the samples is confirmed by the two typical Si-O-Si asymmetrical stretching bands centered at 1100 cm^{-1} and 1025 cm^{-1} in the FTIR spectra (Supporting information, Figure S2) [32]. According to the literature [33], the strong relative intensity of the band at 1025 cm^{-1} suggests a degree of ladder structural irregularity in all samples. A weak band near 3500 cm^{-1} due to O−H stretching vibrations suggest the presence of residual uncondensed Si−OH groups and adsorbed water. All spectra reveal the characteristic carbonyl and vinyl stretching vibrations of the methacrylate groups, at 1716 cm^{-1} at 1637 cm^{-1}, respectively. In addition to the stretching vibrations of aliphatic C−H bonds, MAPSQ(64) and MAPSQ(46) show the C−H stretching bands of phenyl rings.

The ^{29}Si CPMAS NMR spectra of the three ladders are shown in Figure 1a. In accordance with previous results [22], the silicon spectrum of LPMASQ, containing 100% methacrylate pendant groups, exhibits a single peak centered at approximately −67 ppm, corresponding to fully condensed T^3 units, along with a left shoulder at −58 ppm, attributed to T^2 units (approximately 3%, according to ^{29}Si quantitative MAS experiments, not shown). Instead, the ^{29}Si NMR spectra of MAPSQ(64) and MAPSQ(46) (Figure 1a) show two main peaks centered at −68 and −80 ppm, respectively due to the methacryloxypropyl- and the phenyl- substituted Si units, whose relative intensity confirmed the nominal ratio between the silane precursors for both matrices. The propylmethacrylate-substituted T^2 units range from 3% in MAPSQ(64) to 1% in MAPSQ(46) (according to ^{29}Si MAS experiments, not shown). Phenyl T^2 units are not visible since they appear at −70 ppm, as proved by liquid NMR experiments (chemical shift and assignment of the different resonances were checked through ^{29}Si dept NMR experiments in THFd8, not shown). In

conclusion, the silicon-29 analyses confirm a predominantly condensed framework that is in good agreement with the nominal compositions.

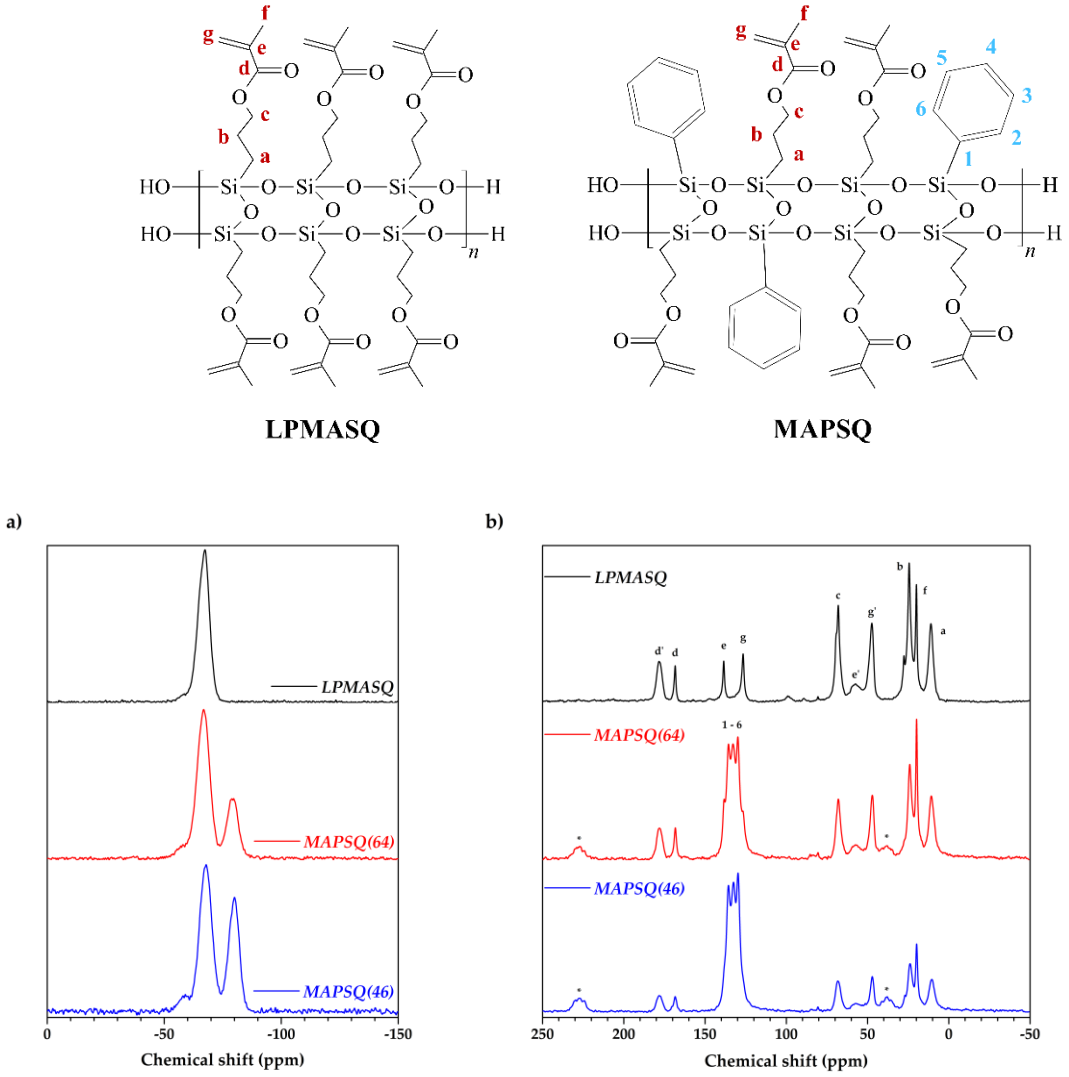

Figure 1: a) ^{29}Si and b) ^{13}C CPMAS NMR spectra of LPMASQ, MAPSQ(64), and MAPSQ(46) photocrosslinked matrices (*: spinning side bands). Carbon labelling is reported on top; structures show the methacrylate functions prior to curing. The schematic representation of the mixed ladders is provided for labeling purposes only and does not reflect the actual distribution of side groups.

The ^{13}C CPMAS NMR spectra (Figure 1b) present all the signals related to the propylmethacrylate functions, as previously observed for LPMASQ sample [34]; in addition, MAPSQ(64) and MAPSQ(46) also show the resonances due to phenyl groups in the range 120–140 ppm. The assignments are indicated in the inset of Figure 1b. These results confirm i) the complete hydrolysis of the alkoxide groups, ii) the nominal composition of the samples, and finally iii) the partial conversion of the methacrylate double bond by photoinduced radical polymerization. This is proved by the presence of an additional carbonyl resonance (d') at about 177 ppm, down-shifted with respect to that of the pristine methacrylate group (d, 165 ppm) [34], and of the resonances (e', g') in the 60–40 ppm range due to the new methylene groups formed at the expense of the methacrylate double bond (e, g). As indicated in our previous works [22, 23], the degree of conversion (DC) of the methacrylate groups can be estimated by the ratio $d'/(d+d') \cdot 100$, where d and d' are the integration areas of the corresponding resonances, resulting in 75%, 67%, and 65% for the LPMASQ, MAPSQ(64), and MAPSQ(46) samples, respectively. The decrease in the degree of methacrylate conversion in MAPSQ(64) and MAPSQ(46) samples is probably determined by the increased distance between the reactive functional groups caused by the copresence of the phenyl groups along the chains.

To further investigate the hindering effect of phenyl groups on the polymerization ability of methacrylate groups, the photopolymerization kinetics of the samples was studied using rt-FTIR analyses, with conversion curves and corresponding polymerization rates presented in Figure 2. rt-FTIR enabled the quantitative monitoring of methacrylate conversion by measuring the decrease in the characteristic olefinic absorption band (at about 1637 cm^{-1}), allowing for a direct assessment of polymerization efficiency and reaction kinetics. LPMASQ and MAPSQ(64) present a comparable overall degree of conversion (Figure 2a), as calculated by Eq.1, as well as a similar

reaction rate (Figure 2b, maximum values of 4 and 5 %·s^{-1}, respectively for MAPSQ(64) and LPMASQ). The MAPSQ(46) matrix, with the highest phenyl content, displays not only the lowest double-bond conversion degree, but also a significantly lower polymerization rate (maximum value of 0.75 %·s^{-1}). These data suggest that the substantial presence of phenyl groups along the ladder chains increases matrix stiffness and viscosity, while decreasing chain mobility and diffusion.

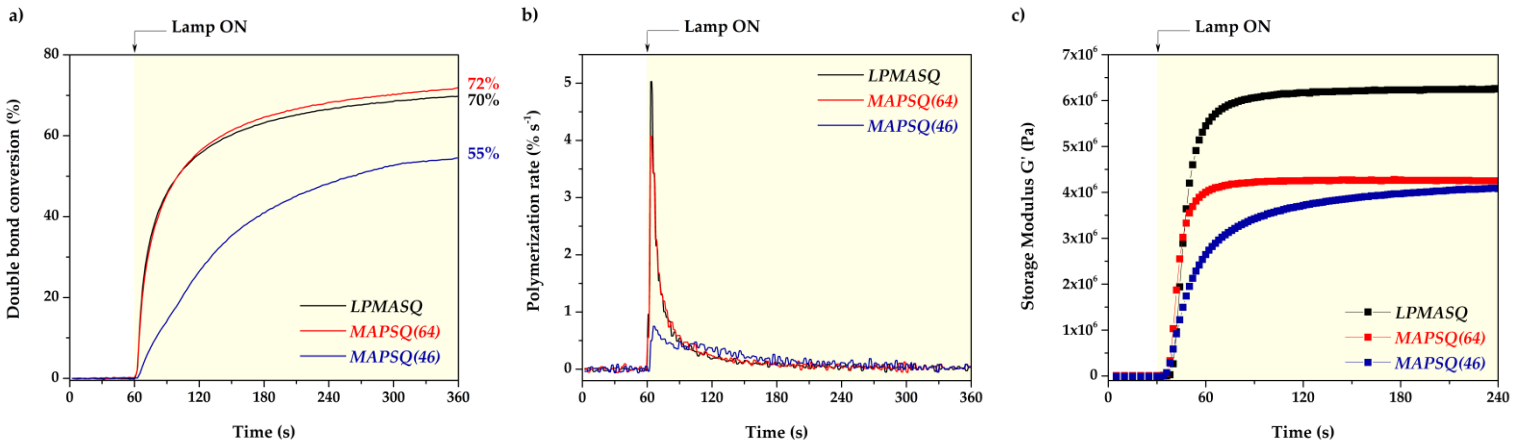

Figure 2: Photocuring kinetics curves of LPSQs samples obtained by real-time FTIR analyses and real-time photorheology experiments: conversion of methacrylate C=C double bonds over time (a) and polymerization rate over time (b) by rt-FTIR spectroscopy; (c) storage modulus over time by photorheology.

It is important to remark that discrepancies between these results and those obtained through NMR can be attributed to differences in irradiation conditions. Specifically, rt-FTIR measurements were performed on sample films approximately 10 µm thick using a lamp intensity of 7 mW·cm^{-2}, whereas NMR spectra were recorded on 300 µm thick samples using a different lamp and intensity (3 mW·cm^{-2}).

Photorheology provided complementary information by monitoring the evolution of the viscoelastic properties during curing. It is important to highlight that the output of these experiments is influenced both by the conversion degree and by the physical interactions of growing macromolecules. Figure 2c illustrates the storage modulus (G') of the matrices as a function of time. LPMASQ and MAPSQ(64) show a steep increase in G' with irradiation time, in agreement with the results shown in Figure 2b; however, the final G' is lower for MAPSQ(64) than for LPMASQ. In contrast, MAPSQ(46) displays a much slower increase in the rate of G' with time, again in accordance with the observed polymerization kinetics, since higher phenyl content increases medium viscosity and hinders the mobility of the reactive propylmethacrylate groups; nevertheless, its final G' value resembles the one of MAPSQ(64). This highlights the contribution of π-π stacking interactions in increasing the network stiffness, in spite of both lower methacrylate conversion and crosslinking degree.

In conclusion, ladders with mixed phenyl-propylmethacrylate side chains exhibit decreased crosslinking by organic polymerization, not only because of the lower availability of methacrylate reactive functions compared to LPMASQ, i.e., 60% for MAPSQ(64) and 40% for MAPSQ(46) respectively, but also because of the inherent obstacles resulting from the random distribution of phenyl groups along the ladder fragments. These results clearly highlight the effects of phenyl group incorporation on matrix rigidity and crosslinking efficiency, which could influence both the microstructural and functional properties of the materials. In line with these findings, preliminary gel content experiments (performed in THF) reveal that the LPMASQ matrix exhibits an insoluble fraction of approximately 99%, confirming very high crosslinking efficiency and the formation of a stable polymer network. The mixed matrices, MAPSQ(64) and MAPSQ(46), also display high insoluble fractions (90% and 92%, respectively), although they retain slightly higher soluble

portions compared to LPMASQ, as expected due to the presence of non-reactive phenyl groups. To evaluate the effect of the organic pendant groups on the structural arrangement of the ladders in the medium-long order range, the X-ray diffraction patterns of the three LPSQs were recorded (Figure 3). Two primary diffraction peaks are observed: one at approximately 2θ ~ 6°, corresponding to the intramolecular periodic chain-to-chain distance (denoted as Y), and another at around 2θ ~ 20°, attributed to the average thickness (denoted as X) of the Si–O–Si silsesquioxane backbone. Additionally, a broad hump centered at 2θ ~ 11° is detected only in LPMASQ, which has been previously associated with the formation of variable side-chain lengths in consequence of the polymerization of the methacrylate groups [34]. From Figure 3 it can be observed that the chain-to-chain distance (Y) decreases with increasing phenyl content: the corresponding peak position changes from about 6.1° to 6.4° to 7.3°, reflecting variations in chain packing density [35]. On the contrary, the average backbone thickness (X) is almost unchanged across the samples.

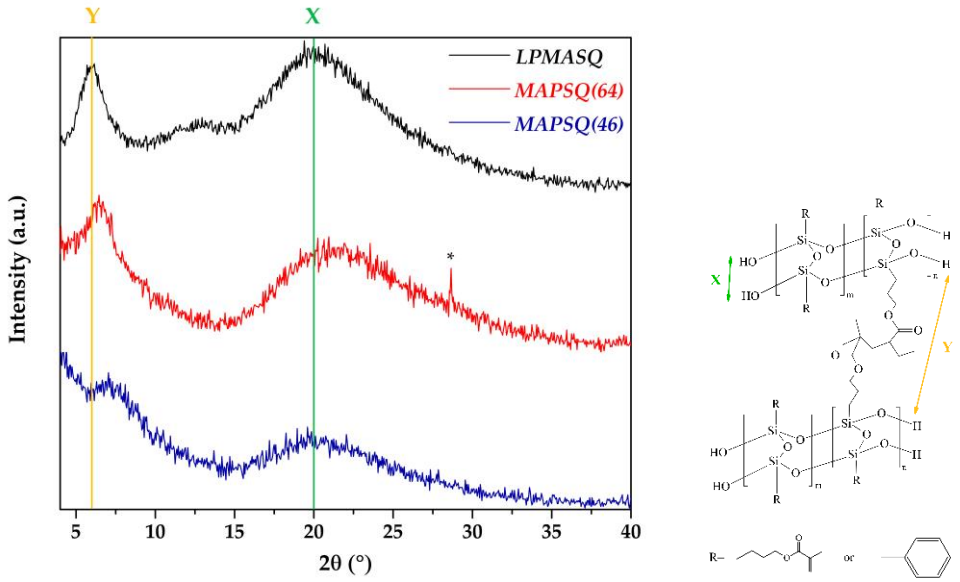

Figure 3: XRD pattern of LPSQs (left) and the schematic structure (right) showing X and Y distances.* : impurity.

Table 2 displays the results of the profile fitting analysis of the experimental patterns: the calculated d-spacing and linewidth (FWHM) of the reflections are reported together with the parameter R, defined as the ratio of the intensities of the Y- and X-related signals ($R=I_Y/I_x$). R provides insights into the structural regularity and defect concentration in LPSQs [34, 36]. For the first peak, the decrease in the d_Y value with increasing the amount of phenyl groups confirms the increase in chain packing density, while the increase in linewidth is related to a broader distribution of intramolecular periodic chain-to-chain distance, likely due to the formation of random copolymers. As the amount of phenyl groups increases, phenyl-rich domains can interact more effectively through π-π stacking. The R value increases with the addition of 40% of phenyl content in the matrix, suggesting the achievement of higher structural regularity. However, a further increase of the percentage of phenyl functions up to 60% reduces the R value to 0.75, which is anyway higher than that of LPMASQ. These findings highlight that the nature of the functional groups affect both molecular packing and structural organization of LPSQs through the combination of covalent and weak interactions among side-chains.

Table 2. Results of the profile fitting analysis of XRD patterns of the three ladder matrices.

Sample	d_Y, nm (FWHM, °)	$d_{Y'}$, nm (FWHM, °)	d_X, nm (FWHM, °)	R (I_Y/I_X)
LPMASQ	1.45 (1.7)	0.74 (3.9)	0.43 (8.4)	0.70
MAPSQ(64)	1.37 (2.0)	-	0.43 (9.0)	0.90
MAPSQ(46)	1.21 (2.7)	-	0.44 (8.1)	0.75

Finally, it is worth noting that the R value obtained for LPMASQ (0.70) is lower than the one obtained (R=0.92) with a lower amount of photoinitiator (1 wt.% with respect to the matrix) in a

previous study [23], where we reported on the effect of photocuring conditions on both methacrylate double bond conversion and configuration of the polymeric chains. In particular, ^{29}Si MAS NMR results showed that using 5% of I-184 photoinitiator not only improved the degree of methacrylate conversion, but also maximized the percentage of linear silsesquioxane chains. From the results obtained in this work, it is possible to assess that the photocuring conditions also affect the structural properties at the scale dimension evaluated by XRD.

3.2 Characterization of LPSQs-Alumina nanocomposites

In order to study in details the effect of the partial substitution in the ladders of the propylmethacrylate side-chains with phenyl groups on filler-matrix interfaces, LPMASQ and MAPSQ(64) matrices were considered for the preparation of nanocomposites. A systematic study on the evolution of structural properties and thermal conductivity behavior was performed by preparing NCs with amounts of Al_2O_3 NPs ranging from 20 to 120 wt.%. NCs were prepared as detailed in section 2.2 by adding NPs functionalized either with MPTMS and APTMS (Table 1), with the aim to investigate the effects of NPs–LPSQs interactions based both on covalent bonds and weak forces. The obtained nanocomposite discs were intact and increasingly opaque as the filler loading increased (Figure S1b).

The successful functionalization of alumina nanoparticles was assessed by FTIR (Figure S3) and SS-NMR(Figure S4) analyses; the silane grafting density was determined from the results of the thermogravimetric analyses (Figure S5), applying a method previously reported [37]. The results of NPs' characterization are described in Supporting information (Section S3).

The influence of alumina nanoparticles on the extent of polymerization of methacrylate groups in the NCs was analyzed using ^{13}C CPMAS NMR spectroscopy (Figure S6). The spectra of NCs

appear very similar to those of the respective matrices (Figure 2b) with no significant peak shifts; thus, the attention was focused on the changes associated with polymerization, which affect the olefinic carbon signals (e, g) with appearance of the new aliphatic e', g' and carbonyl d' resonances. Table 3 reports the degree of methacrylate polymerization in the NCs, quantified from the ratio d'/(d + d'), as detailed in Section 3.1. Clear trends are difficult to find; however, the results indicate that methacrylate polymerization ability results almost unaffected by the incorporation of alumina NPs in MAPSQ(64). Methacrylate conversion in the LPMASQ matrix appears slightly more sensitive to NPs addition, according to previous observations [38, 39]. A general decrease in DC is observed with the highest filler loading (120MA_L and 120AA_L). 120AA_M(64) sample does not appear in line with the trend of M(64)-based NCs, showing a significant decrease in methacrylate polymerization ability.

Despite the similar DC values found for NCs consisting of different ladders, it should be mentioned that the degree of crosslinking is nevertheless lower in MAPSQ(64)-based nanocomposites than in LPMASQ nanocomposites, since only 60% of polymerizable side-chain functions are present.

Table 3. Degree of methacrylate conversion (DC) of LPSQs/Al_2O_3 nanocomposites calculated from ^{13}C CPMAS NMR spectra reported in Figure S6.

Sample ID	DC % (±1)	Sample ID	DC % (±1)
LPMASQ	75%	MAPSQ(64)	67%
20MA_L	69%	20MA_M(64)	67%
40MA_L	68%	40MA_M(64)	67%
80MA_L	72%	80MA_M(64)	68%
120MA_L	69%	120MA_M(64)	68%
20AA_L	65%	20AA_M(64)	69%
40AA_L	70%	40AA_M(64)	69%
80AA_L	70%	80AA_M(64)	68%
120AA_L	67%	120AA_M(64)	59%

The structural changes in LPSQs upon nanoparticle incorporation were also investigated by FTIR spectroscopy (Figure S7, Supporting information). The results do not reveal significant changes, only some variations in the relative intensity of the bands in the siloxane region can be appreciated by increasing the amount of filler, with no clear dependence on NPs functionalization.

To further investigate the effect of filler-matrix interactions on the development of the network, rt-FTIR and photorheology experiments were performed to evaluate the photocrosslinking kinetics of LPMASQ and MAPSQ(64) nanocomposites. The experiments were run on NCs formulations with high nanoparticle loadings, where NPs impact on polymerization and crosslinking behavior is expected to be significant. Nanocomposites containing 80 wt.% functionalized alumina nanoparticles were selected based on previous studies [22, 23], and their behavior was compared

to those of the corresponding matrices. The rt-FTIR data (Figure 4) reveal distinct crosslinking behaviors between LPMASQ and MAPSQ(64) nanocomposites, driven by differences in matrix composition, polymerization kinetics, and interfacial interactions. While the LPMASQ matrix exhibits a double bond conversion of 70% (Figure 2), the addition of methacrylate-functionalized alumina (orange curve, Figure 4a) slightly increases the conversion to 77%, whereas amino-functionalized alumina (green curve, Figure 4a) reduces it to 64%. Notably, the polymerization rate remains nearly constant across all L-based systems (Figure 4b), indicating that nanoparticle incorporation does not significantly influence network formation kinetics or matrix stiffness. These results suggest that in L-based nanocomposites, methacrylate-functionalized alumina is well-integrated within the polymer matrix, whereas amino-functionalized alumina slightly hindered conversion without significant alteration of the system's viscosity or crosslinking dynamics, likely due to filler-filler interactions. MAPSQ(64)-based NCs exhibit a lower double-bond conversion with respect to the matrix (Figure 4d). In fact, the pristine matrix achieves an effective total conversion of 72% (Figure 2), which decreases to 57% in 80MA_M(64) and to 41% in 80AA_M(64). Furthermore, they show a strong reduction of the polymerization rate (Figure 4e). Unlike LPMASQ-based composites, nanoparticle incorporation in M(64)-based systems has a more pronounced effect on polymerization kinetics and stiffness. This is particularly relevant in 80AA_M(64), where the interplay between increased viscosity and nanoparticle-induced interfacial effects further limits methacrylate accessibility and reduces the polymerization rate [40].

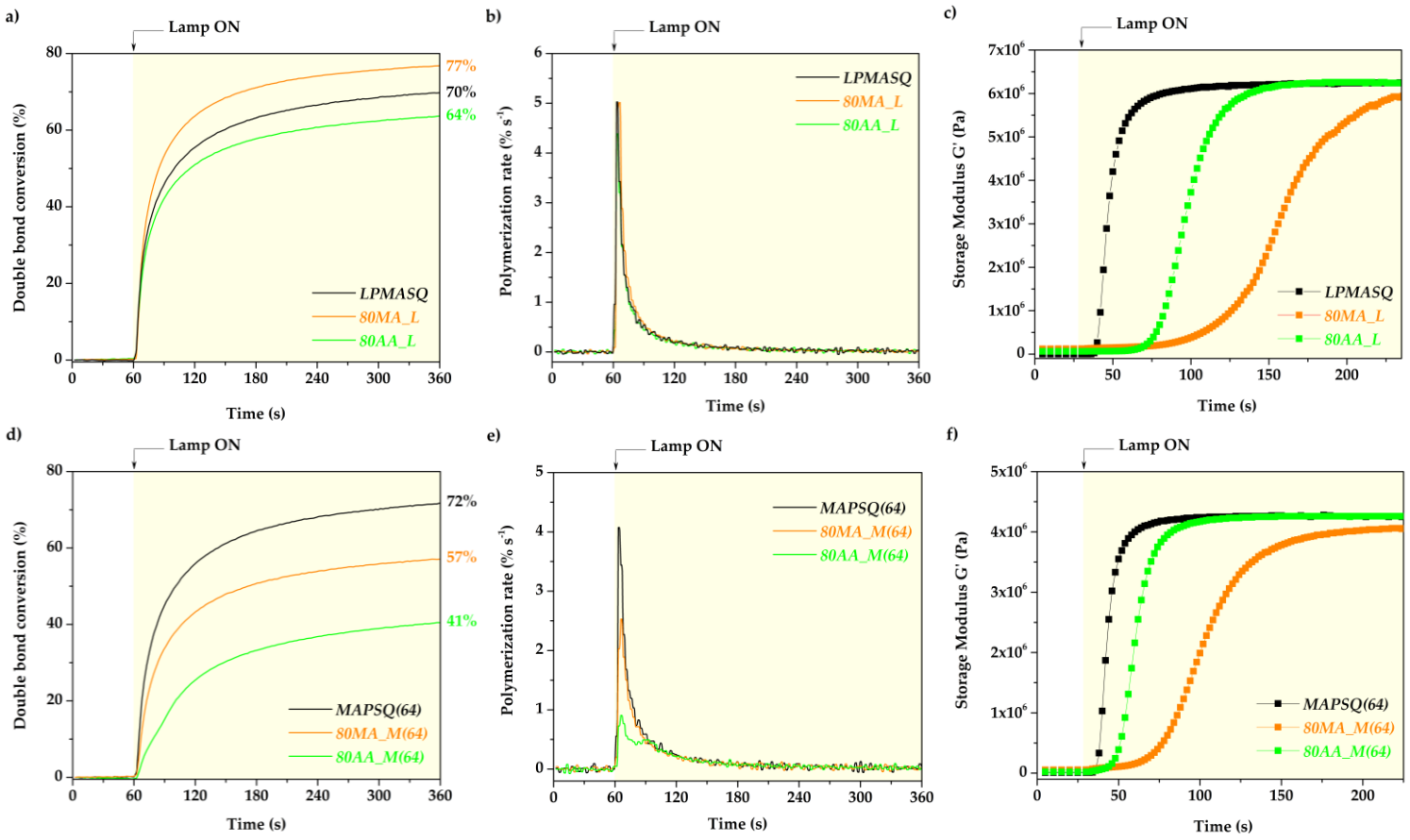

Figure 4: rt-FTIR data displaying (a, d) double bond conversion of methacrylate group over time, and (b, e) polymerization rate over time of pristine matrices and composites filled with 80 wt.% of functionalized alumina nanoparticles; photorheology curves of (c) LPMASQ- and (f) MAPSQ(64)-based nanocomposites with 80 wt.% functionalized NPs.

As underlined in Section 3.1, the experimental conditions used for rt-FTIR experiments reasonably account for the differences between the double-bond conversion values derived from Figure 4 and the DC values reported in Table 3.

The evolution of the NCs' viscoelastic properties during UV-induced polymerization was investigated using photorheology. The time-dependent evolution of the storage modulus (G') is presented in Figures 4c and 4f, tracking the formation of the crosslinked polymeric network. The

increase of G' in the NCs presents a clear delay with respect to the matrices, probably due to the light shielding effect of the ceramic fillers [22, 34]. Furthermore, this shielding effect can also influence the rate of generation of photoactivated species, which in turn influences the degree of methacrylate conversion and not only its rate. Consequently, the final behavior is a complex result of multiple mechanisms, which cannot be defined independently. However, differences in the observed delay are also clearly dependent on NPs functionalization. In fact, 80MA_L and 80MA_M(64) samples present an increase in G' only after 75 and 50 s, respectively, while AA NPs influences the induction period at a lower extent for both matrices. Similarly, nanocomposite samples (colored curves) exhibit a slower increase in G' during irradiation compared to the pristine matrices (black curves), suggesting reduced chain mobility. However, in both matrices, the slope of the curves is lower upon addition of MA nanoparticles (orange curves) than with AA NPs (green curves). It is important to consider that also the dispersion state of the nanofillers (discussed below) can influence the strength of matrix–filler interactions, and consequently, the viscosity of the system [41]. These results suggest that constraints produced by covalent bonding could interfere with the network formation. Indeed, covalent bonds can be formed both between polymer chains and nanoparticles, and among functionalized nanoparticles. Therefore, the overall behavior of NCs appears strongly dictated by a balance between filler-matrix and filler-filler interactions. On the other hand, AA particles exhibit a distinct behavior as evidenced by the steeper increase in G'. This suggests that despite the lower chemical conversion, the polymer chains may still achieve sufficient crosslinking to quickly form a rigid structure, likely due to weak interfacial interactions between the matrix and the filler. Preliminary gel content measurements in THF revealed that the nanocomposites exhibit high insoluble fractions, similar to those of their respective matrices, regardless of the type of nanofiller, confirming their stability and chemical resistance. The

microstructural features of the nanocomposites with 80 wt.% alumina loadings were analyzed using both XRD and SEM. As previously reported [23], this composition was selected as representative of NCs with high filler loadings, allowing the evaluation both of filler and matrix features. The comparison among XRD patterns of NCs containing 80 wt.% of functionalized NPs and the corresponding matrices is presented in Figure S8. NCs show the crystalline reflections of alumina in the range $2\theta = 30–40°$, and display modifications in shape and intensity of the silsesquioxane halos. Table S1 reports the calculated parameters obtained from the profile fitting of the experimental patterns. The presence of propylmethacrylate and aminopropyl groups on alumina surface leads to different effects on ladders, namely the variation of chain packing (Y distance), and the modification of structural regularity (R value). The most relevant effects are found embedding aminopropyl-functionalized NPs into LPMASQ and propylmethacrylate-functionalized NPs into MAPSQ(64). The increase in R, namely in the structural regularity, coupled with the increase in chain-to-chain distance (Y) is observed in 80AA_L. This suggests that filler-filler and filler-matrix weak interactions, such as H-bonding or dipolar forces, could have contributed to a more regular arrangement of polymerized ladders chains, as suggested also by the disappearance of the broad hump (centered at $2\theta \sim 11°$). In contrast, MA NPs strongly disturb the structural regularity of MAPSQ(64) chains, according to the decrease in the R value. The possible formation of covalent bonds between methacrylate groups of ladders and particles also interferes with the π-π stacking, probably accounting for the high chain packing observed in the pristine matrix, thus leading to an increase in Y distance. On the other hand, R values of 80MA_L and 80AA_M(64) samples evidence that adding few covalent bonds in a network with prevailing strong chemical interactions (LPMASQ) or increasing the extent of the weak

interactions in a network characterized by effective π-π interactions (MAPSQ(64)) only slightly modify ladder structure regularity.

SEM images of NCs' cross-sectional surfaces (Figure 5) reveal a generally homogeneous filler dispersion across all samples, although a certain extent of nanoparticle aggregation is observed. As previously reported [22, 23], the functionalized alumina nanoparticles are effectively embedded within both matrices, with only minor variations among the different samples. Both the absence of defects and homogeneous particle distribution are detected in sample 80MA_L (Figure 5a) owing to the high chemical compatibility provided by the presence of the same functional groups in the ladders and particles. Only few pores are visible in the NCs, but samples containing AA particles (Figure 5b and d) exhibit small regions devoid of filler, suggesting the occurrence of some phase separation during processing. Therefore, strong polymer-filler interactions resulted in improved filler dispersion.

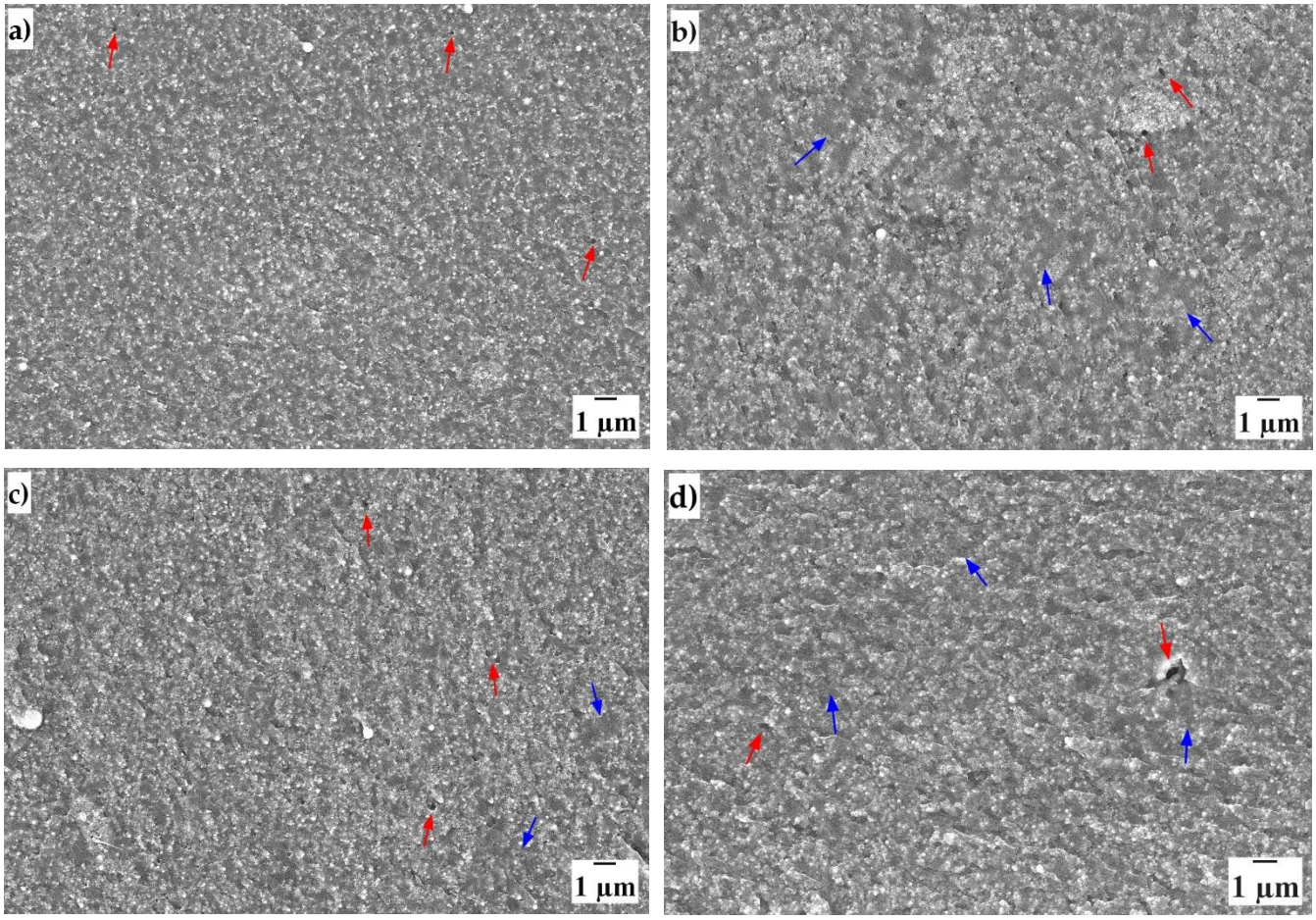

Figure 5: SEM micrographs at 10kX magnification of (a) 80MA_L, (b) 80AA_L, (c) 80MA_M(64), and (d) 80AA_M(64) nanocomposites. Red arrows indicate pores, while blue arrows highlight depleted regions.

The thermal stability of matrices and nanocomposites was assessed through TGA in air (Figure S9). All samples show similar degradation curves, but the introduction of the phenyl groups in the matrix leads to less sharp mass loss steps with respect to LPMASQ, probably because of a random distribution of the two functionalities along ladders' chains. In addition, the lower decomposition temperature (T_d, i.e. the temperature corresponding to 5% weight loss) of MAPSQ(64) sample (341 °C) with respect to LPMASQ (359 °C) could be related to the reduced degree of methacrylate polymerization. Finally, the residual mass at 950 °C was higher for MAPSQ(64) (41%) than for

LPMASQ (34%), confirming previous findings [16, 25, 29] . As expected, in the NCs the net weight loss decreases with increasing filler concentration. T_d increases by increasing filler concentrations, starting from 40 wt.% loading. In NCs with the highest filler content, T_d values range from 383 °C for 120MA_L to 394 °C for 120AA_L, while both composites made of M(64) matrix show a value of 387 °C; net weight losses for NCs samples are similar (about 30%). It should be noted that both LPSQs' thermal stability [15, 16] and the improvement in thermal behavior resulting from the addition of high loadings of ceramic NPs are positive aspects for ladder-based NCs application as thermal management materials.

Thermal conductivity of both matrices and nanocomposites was evaluated from the values of density, specific heat capacity and thermal diffusivity (Table S2) using Eq.2, as described in Section 2.3. Despite the lower methacrylate conversion and reduced crosslinking degree (due to the presence of a lower amount of polymerizable groups), MAPSQ(64) presents a slightly higher density than LPMASQ, suggesting that chain packing could benefit from the occurrence of π-π interactions between the phenyl groups. Density (ρ) progressively increases with increasing filler loading, in agreement with the lower amount of defects observed in the cross-section surfaces (Figure 5). As expected, the thermal diffusivity (α) increases and heat capacity (c_P) decreases as the filler concentration increased. A linear increase of TC as a function of alumina volume fraction (Al_2O_3 vol.%) is observed (Figure 6).

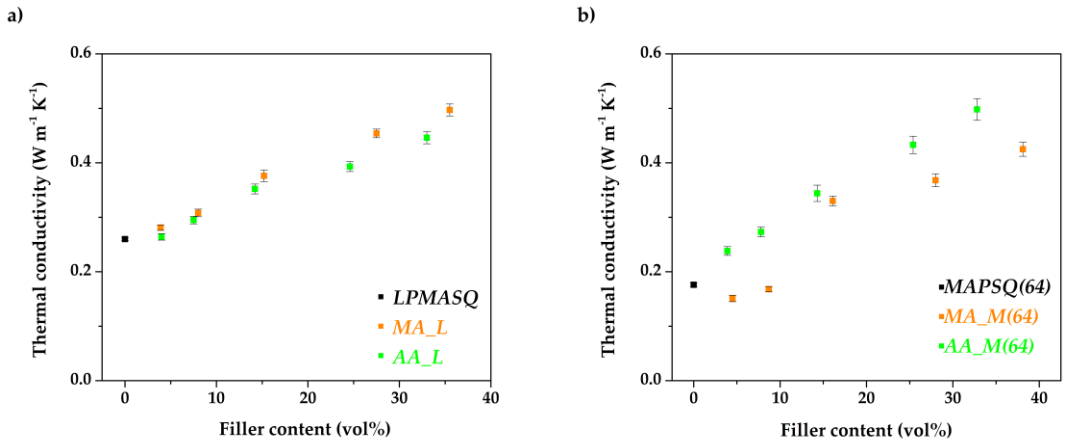

Figure 6: TC evolution of (a) LPMASQ-based and (b) MAPSQ(64)-based composites with respect to alumina volume percentage.

The calculated TC values for the nanocomposites with high filler content and the corresponding percentage gain relative to the crosslinked matrices are summarized in Table 4. It is worth noting that these NCs exhibit significant TC and thermal stability compared to silicon rubber-based systems [42–44] with similar filler loading.

Table 4. Thermal conductivity (k) of LPMASQ- and MAPSQ(64)-based nanocomposites with high filler content (i.e. 80 and 120 wt.%); the TC gain with respect to their relative matrices is also reported.

Sample	k ($W \cdot m^{-1} \cdot K^{-1}$)	TC gain (%)		Sample	k ($W \cdot m^{-1} \cdot K^{-1}$)	TC gain (%)
LPMASQ	0.260 ± 0.003	-		MAPSQ(64)	0.176 ± 0.003	-
80MA_L	0.454 ± 0.008	+74.6		80MA_ M(64)	0.368 ± 0.012	+109.1
120MA_L	0.497 ± 0.011	+91.2		120MA_ M(64)	0.425 ± 0.013	+141.5
80AA_L	0.393 ± 0.009	+51.2		80AA_ M(64)	0.433 ± 0.016	+146.0
120AA_L	0.446 ± 0.011	+71.5		120AA_ M(64)	0.498 ± 0.020	+183.0

MAPSQ(64) matrix presents lower TC (0.176 $W \cdot m^{-1} \cdot K^{-1}$) than LPMASQ (0.260 $W \cdot m^{-1} \cdot K^{-1}$), probably due to both lower crosslinking degree, related to the presence of 40% non-polymerizable phenyl groups, and lower DC (Table 3) with respect to LPMASQ. The correlation between methacrylate polymerization ability and TC can be extended to L-nanocomposites containing MA nanoparticles, where covalent bonding with the matrix could occur. Specifically, the 120MA_L sample reaches a TC value of 0.497 $W \cdot m^{-1} \cdot K^{-1}$, significantly higher than its MAPSQ(64) counterpart (120MA_M(64): 0.425 $W \cdot m^{-1} \cdot K^{-1}$). This suggests that covalent interactions between MA particles and the crosslinked polymer network could enhance the TC by creating a suitable path for phonon transport. rt-FTIR data supports this hypothesis: in L-based composites, the polymerization rate (Figure 4) remains largely unaffected by nanoparticle incorporation, suggesting that MA particles are partially integrated by covalent bonds into the crosslinked matrix.

Conversely, the trend reverses for composites embedding AA particles, where weak interactions should dominate. MAPSQ(64)-based composites exhibit higher TC values than the LPMASQ analogs. In particular, the TC value of 120AA_M(64) (0.498 $W \cdot m^{-1} \cdot K^{-1}$) is higher than that of 120AA_L (0.446 $W \cdot m^{-1} \cdot K^{-1}$), highlighting the role of phenyl-mediated interfacial interactions in improving phonon transport, despite the lower crosslinking density of MAPSQ(64).

Furthermore, 120AA_M(64) and 120MA_L display comparable TC values with significantly greater TC gain with respect to the respective matrices (+183% and +91.2%, respectively). This suggests that the optimized weak interactions in MAPSQ(64)-based composites can compensate for the lack of covalent bonding and achieve similar thermal transport efficiency.

To further explore the influence of weak interfacial interactions on TC, two nanocomposite samples containing 80 wt.% functionalized alumina nanoparticles were prepared using the MAPSQ(46) matrix. As reported in Section 3.1, MAPSQ(46) was characterized by lower degree

of methacrylate conversion than MAPSQ(64), and its overall extent of polymerization was reduced, due to the availability of only 40% of reactive groups on the ladder chains. Therefore, weak interactions are expected to increase in this ladder matrix, which contains more phenyl groups while maintaining a partially crosslinked structure, with expected effects on phonon transport.

rt-FTIR data for the MAPSQ(46)-based systems indicate both less effective double-bond conversion (Figure S10a) and decrease in the polymerization rate (Figure S10b) compared to analogous composites based on MAPSQ(64) matrix (Figure 4). Notably, 80MA_M(46) sample exhibits a higher polymerization rate than the pristine MAPSQ(46) film, probably due to the covalent interactions between MA particles and the methacrylate groups in the matrix. Photorheology results (Figure S10c) follow a trend similar to those previously observed (Figure 4): MA particles delays polymerization probably due to covalent bonding with methacrylate chain-groups, restricting chain mobility; in contrast, AA-filled nanocomposite exhibits a steeper G' increase, quickly forming a rigid structure thanks to weak interactions.

The SEM image of the cross-section surface of 80MA_M(46) composite (Figure 7a) displays a quite homogeneous NPs' dispersion, thus confirming the conclusions of the polymerization study. It is noteworthy that 80AA_M(46) sample (Figure 7b) shows more pronounced agglomeration and larger areas of depletion than the analogous sample prepared from MAPSQ(64) (Figure 5d).

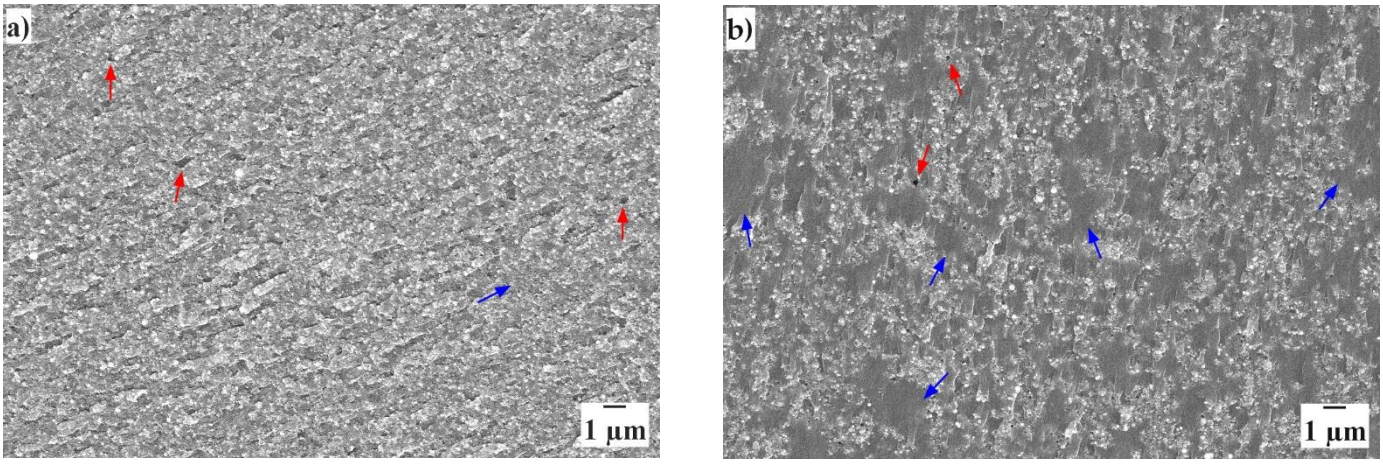

Figure 7: SEM micrographs at 10kX magnification of (a) 80MA_M(46) and (b) 80AA_M(46). Red arrows indicate pores, while blue arrows highlight depleted regions.

Finally, TGA of MAPSQ(46) matrix (Figure S11) reveal that both T_d (346°C) and residual mass (49 wt.%) are higher than those of MAPSQ(64). As previously observed, the addition of nanoparticles further improves the thermal stability of the samples.

Table S3 presents the density, specific heat capacity, thermal diffusivity, and thermal conductivity values of the MAPSQ(46) matrix and nanocomposites, whereas Figure 8 compares their TC values calculated using Eq.2 with those of the other ladder matrices and corresponding nanocomposites. A further increase in density with respect to MAPSQ(64) is observed for MAPSQ(46). It is worth noting the large increase in thermal diffusivity compared to the matrix with lower phenyl amount, reaching a value (0.1456 $mm^2 \cdot s^{-1}$) almost comparable to that of LPMASQ, which leads to a valuable increase in TC (Table S3). In spite of the lower network crosslinking due to the limited polymerization, larger domains with enhanced π-π stacking interactions in MAPSQ(46) may contribute to a more densely packed structure that could facilitate heat transfer.

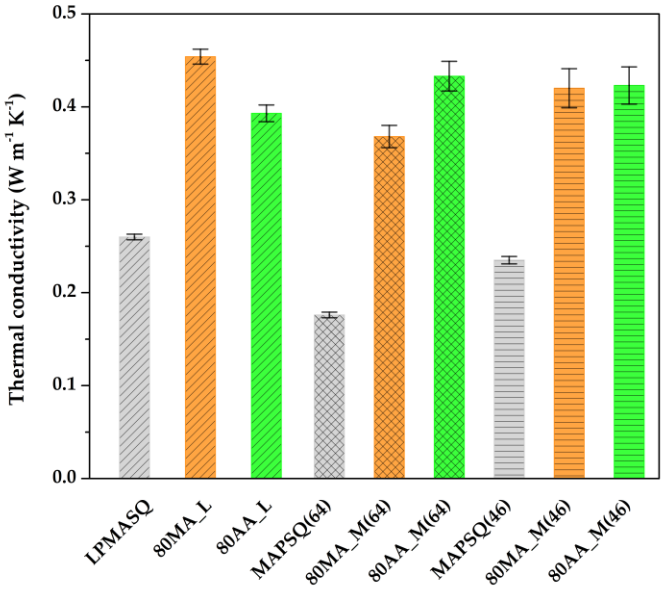

Figure 8: Comparison of the thermal conductivities of the matrices and 80 wt. % alumina filled NCs.

M(46)-based NCs display remarkable TC values compared with both M(64) and L-based samples: the TC of 80MA_M(46) is only slightly lower than that of 80MA_L, and 80AA_M(46) presents a value comparable to that of 80AA_M(64). Multiple factors influence phonon transport: enhanced π-π stacking interactions may contribute to a more interconnected structure that facilitate heat transfer, but crosslinking density, molecular packing and NPs distribution can further impact phonon pathways. Even though the degree of crosslinking is lower, due to only 40% of available reactive functions, the density values of 80MA_M(46) and 80MA_M(64) are identical, probably because interactions among phenyl groups are likely more effective, and NPs distribution is quite homogeneous. In contrast, in the case of 80AA_M(46), the existence of large regions depleted of NPs, as observed by SEM (Figure 7b), can reduce the improvement in heat transfer provided by the ceramic particles.

4. Conclusions

Nanocomposites made of LPSQs presenting both methacrylate and phenyl side groups and Al_2O_3 NPs functionalized with methacrylate or amino groups were produced by solvent casting and UV curing. Both photopolymerization kinetics (by rt-FTIR and photorheology measurements) and degree of methacrylate conversion (^{13}C NMR) were evaluated in relation to the methacrylate/phenyl molar ratio and the amount and functionalization of fillers. The effect of these parameters on the structure and thermal conductivity of matrices and nanocomposites was investigated. The results demonstrate that the TC is strongly influenced by filler-matrix interactions, polymerization ability, and structural organization at the molecular level. Among the matrices, LPMASQ exhibited the highest TC (0.260 $W \cdot m^{-1} \cdot K^{-1}$), attributed to its higher extent of methacrylate conversion and network crosslinking. In contrast, despite lower methacrylate conversion and crosslinking degree, MAPSQ(46) showed a TC of 0.235 $W \cdot m^{-1} \cdot K^{-1}$, likely due to the large phenyl content (60%), which promotes π-π stacking interactions and the formation of a more densely packed structure that favors heat transfer. Although more crosslinked, MAPSQ(64) presents a reduced TC value (0.176 $W \cdot m^{-1} \cdot K^{-1}$), suggesting that the distribution of phenyl groups along the chains does not allow a synergistic effect between covalent and weak interactions.

MA-functionalized nanoparticles were well-dispersed in the NCs, while AA-functionalized nanoparticles showed less compatibility with the matrices, leading to the appearance of regions depleted of NPs with a dependence on the amount of phenyl side groups. The addition of MA-NPs to LPMASQ-based systems led to a valuable increase in TC, reaching a value of 0.497 and 0.454 $W \cdot m^{-1} \cdot K^{-1}$ for 120MA_L and 80MA_L respectively, due to both high particles dispersion and copolymerization with the matrix. The corresponding samples based on MAPSQ(64) performed

less well (0.368 $W \cdot m^{-1} \cdot K^{-1}$ and 0.425 $W \cdot m^{-1} \cdot K^{-1}$ for 80MA_M(64) and 120MA_M(64), respectively). However, 80MA_M(46) exhibited a significant TC value (0.420 $W \cdot m^{-1} \cdot K^{-1}$) , suggesting that the extended π-π stacking domains effectively contributed to phonon transport despite reduced polymerization. The comparison of nanocomposites comprising AA NPs points out contrasting behaviors: while weak interfacial interactions in 80AA_L led to lower TC, systems based on mixed methacrylate-phenyl ladders showed enhanced TC, but the effect of interactions introduced by the amino groups was more effective in MAPSQ(64) than in MAPSQ(46). The increased chain-to-chain distance (Y) and R value in 80AA_L suggest that weak interactions due to the amino groups affected the polymer chain conformation, probably introducing phonon-scattering sites that limited heat conduction. Indeed, 80AA_L exhibited a lower TC than 80MA_L despite sharing a similar degree of methacrylate conversion. Conversely, AA nanoparticles contributed to boosting the thermal diffusivity in mixed ladders, suggesting that improving weak interactions could play a beneficial role in matrices with a reduced extent of polymerization.

Notably, the NCs exhibited good thermal stability in addition to a valuable TC, confirming their suitability for applications requiring enhanced heat dissipation. This study highlights the complex interplay between molecular interactions, crosslinking behavior, and thermal conductivity in ladder polysilsesquioxane-based matrices and their nanocomposites. The results reveal the importance of balancing covalent and weak interactions to optimize the TC in NCs by manipulating the particle surface functionalization and the nature of the pending groups in ladder-like polysilsesquioxanes. These findings provide useful insights for the design of novel thermal management materials suitable for application in flexible electronics.

Acknowledgment

This work was performed in the frame of the program Departments of Excellence 2023-2027 (DII-UNITN)—Italian Ministry of University and Research (MUR).

Author contributions: CRediT

Chiara Romeo: Investigation, Conceptualization, Validation, Data Curation, Writing – original draft. **Emanuela Callone:** Resources, Data Curation. **Riccardo Ceccato:** Resources, Data Curation. **Francesco Parrino:** Supervision, Conceptualization, Writing – review & editing. **Giulia Fredi:** Resources, Writing – review & editing. **Alessandra Vitale:** Resources, Writing – review & editing. **Ignazio Roppolo:** Resources, Writing – review & editing. **Roberta Bongiovanni:** Resources, Writing – review & editing. **Massimiliano D'Arienzo:** Conceptualization, Writing – review & editing. **Sandra Dirè:** Supervision, Conceptualization, Writing – review & editing.

Appendix A. Supplementary data

Supplementary data to this article can be found online at…

References

[1] Z. M. Zhang, Z. M. Zhang, Luby. Nano/Microscale Heat Transfer, 2nd ed.; Springer Nature, Cham, Switzerland, 2020.

[2] H. Chen, V. V. Ginzburg, J. Yang, Y. Yang, W. Liu, Y. Huang, L. Du, B. Chen, Thermal conductivity of polymer-based composites: Fundamentals and applications, Prog. Polym. Sci. 59 (2016) 41-85. https://doi.org/10.1016/j.progpolymsci.2016.03.001

[3] B. Tonpheng, J. Yu, O. Andersson, Effects of cross-links, pressure and temperature on the thermal properties and glass transition behaviour of polybutadiene, Phys. Chem. Chem. Phys. 13 (2011) 15047-15054. https://doi.org/10.1039/C1CP20785G

[4] J. Li, X. Zhang, M. M. F. Yuen, L. Liu, C. S. Ku, K. Zhang, Enhancing the thermal conductivity of silicone composites by increasing crosslink degree. 15th International Conference on Electronic Packaging Technology. Proceedings of the ICEPT 2014, Chengdu, China, August 12-15, 2014; IEEE Xplore, 2014, pp 329-333.

[5] Y. Li, C. Gong, C. Li, K. Ruan, C. Liu, H. Liu, J. Gu, Liquid crystalline texture and hydrogen bond on the thermal conductivities of intrinsic thermal conductive polymer films, J. Mater. Sci. Technol. 82 (2021) 250–256. https://doi.org/10.1016/j.jmst.2021.01.017

[6] C. Huang, X. Qian, R. Yang, Thermal conductivity of polymers and polymer nanocomposites, Mater. Sci. Eng.: R: Rep. 132 (2018) 1-22. https://doi.org/10.1016/j.mser.2018.06.002

[7] A. R. J. Hussain, A. A. Alahyari, S. A. Eastman, C. Thibaud-Erkey, S. Johnston, M. J. Sobkowicz, Review of polymers for heat exchanger applications: Factors concerning thermal conductivity, Appl. Therm. Eng. 113 (2017) 1118-1127. https://doi.org/10.1016/j.applthermaleng.2016.11.041

[8] T. Yao, C. Zhang, Z. Zhang, T. Niu, Q. Yi, Y. Yang, Hydrogen bonding and π-π interaction enhanced high thermal interface design with low dielectric loss of BN/PI/epoxy for high voltage-

high frequency insulating application, Adv. Compos. Hybrid Mater. 7 (2024) 30. https://doi.org/10.1007/s42114-023-00826-x

[9] H. Ma, B. Gao, M. Wang, Z. Yuan, J. Shen, J. Zhao, Y. Feng, Strategies for enhancing thermal conductivity of polymer-based thermal interface materials: A review, J. Mater. Sci. 56 (2021) 1064-1086. https://doi.org/10.1007/s10853-020-05279-x

[10] L. Mirizzi, M. D'Arienzo, R. Nisticò, G. Fredi, S. Diré, E. Callone, A. Dorigato, L. Giannini, S. Guerra, S. Mostoni, B. Di Credico, R. Scotti, Al_2O_3 decorated with polyhedral silsesquioxane units: An unconventional filler system for upgrading thermal conductivity and mechanical properties of rubber composites, Compos. Sci. Technol. 236 (2023) 109977. https://doi.org/10.1016/j.compscitech.2023.109977

[11] S. Dirè, E. Borovin, F. Ribot, Architecture of Silsesquioxanes, in: L. Klein, M. Aparicio, A. Jitianu (Eds.), Handbook of Sol-Gel Science and Technology: Processing, Characterization and Applications, Springer International Publishing, Cham, 2016, pp 1-34.

[12] A. S. Lee, S. S. Choi, K. Y. Baek, S. S. Hwang, Hydrolysis kinetics of a sol-gel equilibrium yielding ladder-like polysilsesquioxanes, Inorg. Chem. Commun. 73 (2016) 7-11. https://doi.org/10.1016/j.inoche.2016.09.004

[13] R. H. Baney, M. Itoh, A. Sakakibara, T. Suzuki, Silsesquioxanes, Chem. Rev. 95 (1995) 1409-1430. https://doi.org/10.1021/cr00037a012

[14] S. W. Kuo, F. C. Chang, POSS related polymer nanocomposites, Prog. Polym. Sci. 36 (2011) 1649-1696. https://doi.org/10.1016/j.progpolymsci.2011.05.002

[15] Z. Li, Ladder Polysiloxanes, in: Y. Xia, M. Yamaguchi, T. Y. Luh, (Eds.), Ladder Polymers: Synthesis, Properties, Applications, and Perspectives, John Wiley & Sons, 2023, pp 285-300.

[16] J. Kim, Y. Park, M. S. Kwon, Recent progress in ladder-like polysilsesquioxane: Synthesis and applications, Mater. Chem. Front. 8 (2024) 2689-2726. https://doi.org/10.1039/D4QM00197D

[17] A. S. Lee, Y. Y. Jo, H. Jeon, S. S. Choi, K. Y. Baek, S. S. Hwang, Mechanical properties of thiol-ene UV-curable thermoplastic polysilsesquioxanes, Polymer 68 (2015) 140-146. https://doi.org/10.1016/j.polymer.2015.05.007

[18] S. Park, J. Y. Kim, W. Choi, M. J. Lee, J. Heo, D. Choi, S. Jung, J. Kwon, S. H. Choi, J. Hong, Ladder-like polysilsesquioxanes with antibacterial chains and durable siloxane networks, Chem. Eng. J. 393 (2020) 124686. https://doi.org/10.1016/j.cej.2020.124686

[19] N. Ahmed, H. Fan, P. Dubois, X. Zhang, S. Fahad, T. Aziz, J. Wan, Nano-engineering and micromolecular science of polysilsesquioxane materials and their emerging applications, J. Mater. Chem. A 7 (2019) 21577-21604. https://doi.org/10.1039/C9TA04575A

[20] M. D'Arienzo, S. Diré, V. Masneri, D. Rovera, B. Di Credico, E. Callone, S. Mascotto, A. Pegoretti, F. Ziarelli, R. Scotti, Tailoring the Dielectric and Mechanical Properties of Polybutadiene Nanocomposites by Using Designed Ladder-like Polysilsesquioxanes, ACS Appl. Nano Mater. 1 (2018) 3817-3828. https://doi.org/10.1021/acsanm.8b00558

[21] J. Bai, H. Fan, Q. Ke, F. Luo, J. Chen, L. Peng, Y. Ding, J. Zhang, G. Zhang, M. Yang, High performance epoxy composites modified by a ladder-like polysilsesquioxanes, Compos. Commun. 46 (2024) 101813. https://doi.org/10.1016/j.coco.2024.101813

[22] P. Mingarelli, C. Romeo, E. Callone, G. Fredi, A. Dorigato, M. D'Arienzo, F. Parrino, S. Dirè, Ladder-like Poly (methacryloxypropyl) silsesquioxane-Al_2O_3-polybutadiene Flexible Nanocomposites with High Thermal Conductivity, Gels 9 (2023) 810. https://doi.org/10.3390/gels9100810

[23] C. Romeo, G. Fredi, E. Callone, F. Parrino, S. Dirè, Effect of Photo-Crosslinking Conditions on Thermal Conductivity of Photo-Curable Ladder-like Polysilsesquioxane–Al_2O_3 Nanocomposites, J. Compos. Sci. 8 (2024) 295. https://doi.org/10.3390/jcs8080295

[24] Y. H. Kim, G. M. Choi, J. G. Bae, Y. H. Kim, B. S. Bae, High-performance and simply-synthesized ladder-like structured methacrylate siloxane hybrid material for flexible hard coating, Polymers 10 (2018) 449. https://doi.org/10.3390/polym10040449

[25] S. S. Choi, A. S. Lee, H. S. Lee, H. Y. Jeon, K. Y. Baek, D. H. Choi, S. S. Hwang, Synthesis and characterization of UV-curable ladder-like polysilsesquioxanes, J. Polym. Sci. Part A: Polym. Chem. 49 (2011) 5012-5018. https://doi.org/10.1002/pola.24942

[26] Z. Zhang, Y. Huang, Q. Xie, G. Liu, C. Ma, G. Zhang, Functional Polymer–Ceramic Hybrid Coatings: Status, Progress, and Trend, Prog. Polym. Sci. (2024) 101840. https://doi.org/10.1016/j.progpolymsci.2024.101840

[27] M. H. Choi, J. Y. Seo, J. Ahn, H. Y. Woo, S. Cho, S. S. Hwang, A. S. Lee, K. Y. Baek, Flowable polysilsesquioxanes as robust solvent-free optical hard coatings, React. Funct. Polym. 167 (2021) 105030. https://doi.org/10.1016/j.reactfunctpolym.2021.105030

[28] A. S. S. Lee, S. S. Choi, H. S. Lee, H. Y. Jeon, K. Y. Baek, S. S. Hwang, Synthesis and characterization of organic–inorganic hybrid block copolymers containing a fully condensed

ladder-like polyphenylsilsesquioxane, J. Polym. Sci. Part A: Polym. Chem. 50 (2012) 4563-4570. https://doi.org/10.1002/pola.26269

[29] W. Zhang, Z. Qin, Y. Lan, X. Zhang, W. Zhang, Y. Pan, R. Yang, Flame retardant composites of ladder phenyl/vinyl polysilsesquioxane-reinforced vinyl ester, J. Mater. Sci. 56 (2021) 457-473. https://doi.org/10.1007/s10853-020-05281-3

[30] T. Hamada, T. Goto, S. Takase, K. Okada, A. Uedono, J. Ohshita, Structure–thermal property relationships of polysilsesquioxanes for thermal insulation materials, ACS Appl. Polym. Mater. 4 (2022) 2851-2859. https://doi.org/10.1021/acsapm.1c01812

[31] Z. Wang, Z. Zeng, H. Li, C. Tang, Properties of ladder-like polysilsesquioxane-modified insulation paper cellulose with different substituents, J. Ind. Eng. Chem. 132 (2024) 437-447. https://doi.org/10.1016/j.jiec.2023.11.036

[32] Y. Sato, R. Hayami, T. Gunji, Characterization of NMR, IR, and Raman spectra for siloxanes and silsesquioxanes: a mini review, J. Sol-Gel Sci. Technol. 104 (2022) 36-52. https://doi.org/10.1007/s10971-022-05920-y

[33] A. S. S. Lee, J. H. Lee, J. C. Lee, S. M. Hong, S. S. Hwang, C. M. Koo, Novel polysilsesquioxane hybrid polymer electrolytes for lithium ion batteries, J. Mater. Chem. A 2 (2014) 1277-1283. https://doi.org/10.1039/C3TA14290F

[34] S. Dirè, E. Callone, R. Ceccato, F. Parrino, B. Di Credico, S. Mostoni, R. Scotti, M. D'Arienzo, Structural effects of TiO_2 nanoparticles in photocurable ladder-like polysilsesquioxane nanocomposites, J. Sol-Gel Sci. Technol. (2023) 1–13. https://doi.org/10.1007/s10971-023-06127-5

[35] S. O. Hwang, A. S. Lee, J. Y. Lee, S. H. Park, K. I. Jung, H. W. Jung, J. H. Lee, Mechanical properties of ladder-like polysilsesquioxane-based hard coating films containing different organic functional groups, Prog. Org. Coat. 121 (2018) 105-111. https://doi.org/10.1016/j.porgcoat.2018.04.022

[36] S. Pohl, O. Janka, E. Füglein, G. Kickelbick, Thermoplastic Silsesquioxane Hybrid Polymers with a Local Ladder-Type Structure, Macromolecules 54 (2021) 3873–3885. https://doi.org/10.1021/acs.macromol.1c00310

[37] N. Zamperlin, A. Bottacini, E. Callone, A. Pegoretti, M. Fontana, Barium titanate functionalization with organosilanes: Effect on particle compatibility and permittivity in nanocomposites, Molecules 27 (2022) 6499. https://doi.org/10.3390/molecules27196499

[38] M. D'Arienzo, S. Dirè, E. Cobani, S. Orsini, B. Di Credico, C. Antonini, E. Callone, F. Parrino, S.D. Vacche, G. Trusiano, R. Bongiovanni, R. Scotti, SiO_2/ladder-like polysilsesquioxanes nanocomposite coatings: Playing with the hybrid interface for tuning thermal properties and wettability, Coatings 10 (2020) 913. https://doi.org/10.3390/coatings10100913

[39] F. Parrino, M. D'Arienzo, E. Callone, R. Conta, B. Di Credico, S. Mascotto, A. Meyer, R. Scotti, S. Dirè, TiO_2 containing hybrid nanocomposites with active–passive oxygen scavenging capability, Chem. Eng. J. 417 (2021) 129135. https://doi.org/10.1016/j.cej.2021.129135

[40] A. Marcinkowska, D. Przadka, B. Dudziec, K. Szczesniak, E. Andrzejewska, Anchor Effect in Polymerization Kinetics: Case of Monofunctionalized POSS, Polymers 11 (2019) 515. https://doi.org/10.3390/polym11030515

[41] V. Sevriugina, D. Pavliňák, F. Ondreáš, O. Jašek, M. Štaffová, P. Lepcio, Matching low viscosity with enhanced conductivity in vat photopolymerization 3D printing: disparity in the electric and rheological percolation thresholds of carbon-based nanofillers is controlled by the matrix type and filler dispersion, ACS Omega 8 (2023) 45566-45577. https://doi.org/10.1021/acsomega.3c05683

[42] Y. Ouyang, X. Li, F. Ding, L. Bai, F. Yuan, Simultaneously enhance thermal conductive property and mechanical properties of silicon rubber composites by introducing ultrafine Al_2O_3 nanospheres prepared via thermal plasma, Compos. Sci. Technol. 190 (2020) 108019. https://doi.org/10.1016/j.compscitech.2020.108019

[43] J. Song, L. Wu, Y. Zhang, Thermal conductivity enhancement of alumina/silicone rubber composites through constructing a thermally conductive 3D framework, Polym. Bull. 77 (2020) 2139-2153. https://doi.org/10.1007/s00289-019-02839-3

[44] J. P. Cheng, T. Liu, J. Zhang, B. B. Wang, J. Ying, F. Liu, X. B. Zhang, Influence of phase and morphology on thermal conductivity of alumina particle/silicone rubber composites, Appl. Phys. A 117 (2014) 1985-1992.